Analysis of permeability change in dissolving rough fractures using depth-averaged flow and reactive transport models

Lichun Wang[1, 2, 3*], M. Bayani Cardenas[1]

[1] Department of Geological Sciences, University of Texas at Austin, Austin, Texas, USA

[2] now at Institute of Surface-Earth System Science, Tianjin University, Tianjin, 300072, China

[3] Tianjin Key Laboratory of Earth Critical Zone Science and Sustainable Development in Bohai Rim

[*] corresponding author: wanglichun@tju.edu.cn

Highlights:

(1) A 2D depth-averaged flow and reactive transport model is developed for dissolving rough fractures.

(2) The model showed that the linear time-dependence of permeability due to self-reinforcing dissolution is ubiquitous.

(3) The time rate of change of permeability is constant which is consistent with theory and experimental observations.

Key words: Permeability, Fracture, Time, Heterogeneity, Acidic fluid, CO_2

Abstract:

Many geophysical problems and engineering applications involve fluid flow through evolving faults and fractures. These situations are typical in CO_2 injection scenarios where supercritical CO_2 or CO_2–saturated fluids are able to dissolve the solid matrix. Dissolution or precipitation within a fracture could lead to self-reinforcing or self-limiting behavior due to feedbacks from changes in permeability (k). There is limited predictive understanding of this phenomenon. Here, we investigated the case of fracture dissolution using a two-dimensional depth-averaged reactive transport model. The model simulated an acidic fluid dissolving a three-dimensional rough fracture. We observed different dissolution patterns across a wide range of geometric properties and different Peclet and Damkohler numbers (960 cases total). Despite this variation, a persistent linear increase in k with time (t) roughly manifested once the dissolution front advanced through the fracture. The time rate of change of k (k/t) is roughly constant for all simulations. The modeled rate is consistent with a theoretical value based on the parallel plates model and with experimentally derived values. The results confirm the common presence of linear time-dependence of fracture k due to self-reinforcement.

1. Introduction

Fractures are ubiquitous across different scales in subsurface geologic materials (Candela et al., 2012). Mass and energy transport through fractures play a critical role in many geophysical problems, including geothermal exploitation, oil and gas recovery, hydraulic fracturing, and subsurface CO_2 sequestration (Berkowitz, 2002). Transport through fractures is controlled by its intrinsic permeability (k) that is inherently determined by the aperture field (Nicholl et al., 1999; Witherspoon et al., 1980). Fracture aperture fields however are dynamic over broad time scales. Fracture geometry can be altered by mechanical deformation (Kang et al., 2016; Pyrak-Nolte and

Nolte, 2016; Wang and Cardenas, 2016) and mineral dissolution or precipitation (Huerta et al., 2012; Szymczak and Ladd, 2004; Szymczak and Ladd, 2012). Thus, fractures exhibit a broad range of permeability partly due to their evolution.

Here we focused on the problem where an acidic fluid dissolves a rough fracture and leads to *k* and flux increases. This problem is relevant, for example, when vast amounts of CO_2 are injected into a brine-filled reservoir and where potential CO_2 pathways are limited by caprocks (Kampman et al., 2016). However, if fractured caprocks are potentially abundant with calcite or other soluble carbonates, fractures may expand due to dissolution of its walls by the acidic CO_2-saturated brine and reactivity of calcite (Deng et al., 2015). The acidity of brine can be persistently high if CO_2 acts as a separate phase flowing through rough fractures (Fitts and Peters, 2013); this might promote calcitic fracture dissolution, and consequently compromise permanent CO_2 storage (Altman et al., 2014).

Understanding the behavior of calcite fractures exposed to CO_2 and the resultant fracture geometry evolution at the field scale remains challenging; this is due to the scarcity of monitoring data (Fitts and Peters, 2013). Thus, numerous studies turned to physical and numerical experiments to interrogate this problem. Previous experimental studies demonstrated that fracture *k* remains fairly constant unless the reaction front breaks through to the end of fracture (Deng et al., 2015). Regardless of varying CO_2 pressures, dissolution experiments all suggested that fracture *k* increased linearly with time after the reaction front reached the outlet of three-dimensional (3D) fractures. Note that this linear time-dependence of *k* was directly shown in our recent computational study (Wang and Cardenas, 2017) rather than the original experimental study, which only showed that *k* increased with expanding fracture volume instead of directly with time (Deng et al., 2015). These experimental observations motivated our recently proposed theory showing that a linear time-dependence of *k* manifests after the dissolution front reaches the outlet of idealized two-dimensional (2D) fractures (Wang and Cardenas, 2017). However, whether, when, and at what rate *k* increases with time via a linear relationship for natural, 3D, rough, and spatially-correlated fractures remain unaddressed. Moreover, various reactive transport regimes encapsulated by Peclet and Damkohler numbers might affect the dissolution process and thereby alter the response of *k* to fracture dissolution over time. In these situations, the characteristics of *k* evolution are largely unknown. This study addresses these broad unsolved problems related to the fracture *k* evolution.

2. Methods

The approach taken here is to numerically simulate the coupled flow through and dissolution of 3D fractures that consist of pure calcite via a 2D depth-averaged (in-plane) reactive transport model representing Ca^{2+} concentration. The simulations kept track of *k* while the fracture evolves. Synthetic fractures that covered a broad range of geometry (240 cases) with varying roughness and aperture correlation length were analyzed. In total, we implemented 960 reactive transport simulations since we used increasing pressure gradients to achieve different Peclet and Damkohler numbers for each fracture. Note that the Peclet and Damkohler numbers evolve with the fracture aperture field. In this study, the Peclet and Damkohler numbers referred to are the initial values prior to when dissolution begins. For simplicity, a 2D depth-averaged reactive model rather than a 3D model was used here. This is justified by two reasons. First, although a 2D model is unable to generate out-of-plane dissolution, the 2D model can reasonably represent and replicate the reactive transport process within a 3D domain (Detwiler and Rajaram, 2007) (3D computationally-intensive simulations might produce more accurate results (Starchenko et al., 2016)). Therefore, the simulation results of and insights arising from this study can still largely hold. Second, solving a 3D problem involves prohibitive computational expense and instability issues while the 2D model is free of these issues. More detailed explanations follow in section 2.2.

2.1. Generation of synthetic fractures with lognormally distributed aperture

Natural fractures typically have complex spatially-correlated aperture fields following normal and lognormal distributions (Brush and Thomson, 2003; Renshaw, 1995). Here, the spatially-correlated aperture (b) fields with varying dimensionless correlation length ($0.01 \leq \lambda/L \leq 1$ with increment ≈ 0.1, where λ is the correlation length and L ($L = 0.1$m) is total fracture length) were generated through the geostatistical simulator SGeMS via the Sequential Gaussian Model (Remy et al., 2009). The aperture fields originally followed a normal distribution but were converted into a lognormal distribution according to the method proposed by Brush and Thomson (2003), because the lognormal distribution represents a broader range of roughness ($0.1 \leq \sigma_b/\langle b\rangle \leq 1.6$ with increment ≈ 0.2) than the normal distribution could have, where σ_b and $\langle b\rangle$ are the standard deviation and the arithmetic mean of the b field (Figure 1). The b was set to be 1×10^{-12} m wherever contact points were identified. The synthetic fractures were used for assessing the effect of heterogeneity on acidic fluid-induced dissolution patterns via the reactive transport model.

2.2. Two-dimensional (2D) depth-averaged reactive transport model

Previous studies of fracture dissolution due to an acidic fluid have shown that the velocity and concentration fields can reach steady-state much sooner than any appreciable change of aperture field occurs (Detwiler and Rajaram, 2007; Elkhoury et al., 2013). In light of this, we solved the steady-state flow and transport equations for velocity and solute concentration, respectively, and used the resultant concentration for determining the dissolution rate and updating the aperture field. The simulations were implemented sequentially at each time step. That is, we first solved the flow field, followed by the concentration field, and lastly using the Ca^{2+} concentration to update the aperture field. This 2D depth-averaged reactive transport model has been tested to be valid for capturing the dissolution pattern for real 3D fractures (Detwiler and Rajaram, 2007; Elkhoury et al., 2013). The detailed simulation framework is discussed below.

2.2.1. 2D depth-averaged modified Local Cubic Law for fluid flow

Single-phase fluid flow through a fracture is governed by the Navier-Stokes and continuity equations (NSE). Nonetheless, directly solving the NSE for a 3D rough and tortuous fracture flow field is computationally costly and sometimes lead to situations where numerical solvers do not converge, especially for non-Darcian flow situations (Zimmerman et al., 2004; Zimmerman et al., 1991). Vertically-integrating the NSE circumvents having to directly solve the NSE. This approach is valid under certain circumstances such as low pressure gradient cases with small velocity magnitude. In this case when the inertial force in the NSE is negligible, the NSE simplifies into the well-known Local Cubic Law (LCL) upon vertically integrating the local parabolic velocity profile (Nicholl et al., 1999). Thus the LCL is a so-called depth-averaged model (DAM) for fluid flow.

Fracture roughness and tortuosity were separately considered (Brush and Thomson, 2003; Ge, 1997) in the development of previous LCL models. Our recent study improved the prediction of local flow fields through the modified LCL (MLCL) that collectively considered roughness, tortuosity, and weak inertial force (Wang et al., 2015), and thereby the MLCL improves the solution compared to that using other LCL models. The MLCL is:

$$\nabla \cdot \left[\frac{T_x}{M} \frac{\partial p}{\partial x} \cos(\emptyset_x)\, \vec{\imath} + \frac{T_y}{M} \frac{\partial p}{\partial y} \cos(\emptyset_y)\, \vec{\jmath} \right] = 0 \qquad (1)$$

where p [Pa] is total pressure, the transmissivity vector $\boldsymbol{T}$ (T_x, T_y) [m^3] between cells can be estimated using a harmonic mean of adjacent apertures, $\emptyset$ ($\emptyset_x$, $\emptyset_y$) [–] is the flow orientation angle accounting for local tortuosity, M [–] is the correction factor considering roughness and weak inertial force, $\vec{\imath}$ and $\vec{\jmath}$ represent the unit vectors in the x and y directions, respectively. T and $\emptyset$ are estimated based on the aperture field, M can be found at Wang et al. (2015).

In this study, we used the MLCL to solve stead-state fluid flow. We imposed a no-flux boundary for lateral boundaries, and applied a pressure gradient driving fluid flow in the x direction (Figure 2). The resultant p were used for estimating the depth-averaged flux $\boldsymbol{q}$ [q_x, q_y] [m/s]:

$$\boldsymbol{q} = -\frac{b^2}{12\mu}\nabla p \qquad (2)$$

where b [m] is the local aperture, μ [Pa·s] is fluid dynamic viscosity. $\boldsymbol{q}$ was further used for the transport problem which calculated advective and dispersive fluxes. Note that we implemented the simulations by incrementally increasing the pressure gradient (1 Pa/m ~ 1×10^3 Pa/m) to achieve progressively larger flow rates and thus different Peclet and Damkohler numbers for each initial fracture geometry.

2.2.2. 2D depth-averaged advection-dispersion equation for transport

Assuming that the Taylor-Aris' dispersion theory is locally valid (Aris, 1956; Taylor, 1953), the solute transport in 3D rough fractures at steady state can be treated by the 2D depth-averaged model:

$$\nabla \cdot (\boldsymbol{q}C) = \nabla \cdot (b\boldsymbol{D}\boldsymbol{\nabla}C) + R \qquad (3)$$

where b is local aperture field, C [kg/m^3] represents local depth-averaged concentration, i.e., [Ca^{2+}], $\boldsymbol{D}$ [m^2/s] is the dispersion tensor dependent on $\boldsymbol{q}$ according to the Taylor dispersion theory (Wang et al., 2012):

$$\boldsymbol{D} = D_m + \frac{\boldsymbol{q}^2}{210D_m} \qquad (4)$$

The depth-averaged dissolution flux R [kg/(m^{2}s)] is described as (Detwiler and Rajaram, 2007; Szymczak and Ladd, 2012):

$$R = \frac{2\kappa}{1 + \frac{4\kappa b}{Sh \cdot D_m}} \left(C_{eq} - C\right) \qquad (5)$$

where κ is the local chemical reaction rate constant, and C_{eq} [kg/m^3] is the saturated concentration for [Ca^{2+}] when CO_2-saturated brine equilibrates with calcite, Sh ~7.6 [–] is Sherwood number defined as the ratio of dissolution rate to rate of diffusion (Sh is constant for a specific geometry (Kays et al., 2012) given that the fracture length satisfies its threshold requirement), and $D_m = 2.03\times10^{-9}$ m^2/s is the molecular diffusion coefficient. In the case of CO_2-saturated brine dissolving calcite in a relatively low pH environment, κ is on the order of 1×10^{-3} m/s (Elkhoury et al., 2013; Pokrovsky et al., 2009). Given that the mean b is on the order of 1×10^{-3} m, the value of $4\kappa b/(Sh \cdot D_m) \gg 1$, which signifies that equation (5) can be reduced to equation (6) by eliminating κ; i.e., the effect of κ on altering R diminishes (Detwiler and Rajaram, 2007; Wang and Cardenas, 2017).

$$R = \frac{Sh \cdot D_m}{2b} \left(C_{eq} - C\right) \qquad (6)$$

Equation (6) suggests that the entire problem becomes a diffusion-limited system, where R only depends on Ca^{2+} concentration.

The C field was solved through equation (3) for a constant inlet concentration C_{inlet} = 1.22 kg/m^3. The C_{inlet} was smaller than C_{eq}, where C_{inlet} was set to be equilibrated with the invading acidic fluid with a high CO_2 concentration and thus low pH at the inlet, and C_{eq} = 2.10 kg/m^3 following Elkhoury et al. (2013) where pH was higher than that at the inlet. This ensured that dissolution occurs along the invading flow path. Moreover, an open boundary (i.e., no dispersive flux) was specified at the outlet (right) (Figure 2), and the initial C was set to be C_{eq}. The above-mentioned 2D reactive transport scheme with a few assumptions (e.g., constant inlet concentration, the applicability of the Taylor dispersion theory to estimate the local dispersion coefficient) has been verified to be accurate for capturing dissolution patterns within 3D fractures (Detwiler and Rajaram, 2007; Elkhoury et al., 2013).

2.2.3. Updating the dynamic aperture field during dissolution

Based on mass conservation, the expansion rate of the local aperture due to dissolution is:

$$\frac{\partial b}{\partial t} = \frac{R}{F\rho_s} \qquad (7)$$

where t is time, F ($F = 0.4$ [–]) is the stoichiometric coefficient for converting a solid phase mass, i.e. calcite, to aqueous phase, i.e. [Ca^{2+}], and ρ_s [kg/m^3] is solid density. The time step for updating b was determined to ensure that the velocity and concentration fields reach steady-state prior to any appreciable aperture change. That is, at each computational time step, we first solved the steady-state flow field first, and then following this solved the transport equation, and then afterwards used the resultant R for updating b according to equation (7). The simulation kept running until a linear relationship between k and t was observed. This linear relationship is expected for 2D idealized fractures (Wang and Cardenas, 2017). It should follow:

$$k/t = \frac{Sh \cdot D_m}{12F\rho_s}\left(C_{eq} - C\right) \qquad (8)$$

The simulations were implemented in MATLAB via the finite difference method. Specifically, we adopted a central difference approximation for handling the second derivative to achieve second-order accuracy, and applied the upwind scheme for handling the advection term that considers the direction of propagation with first-order accuracy. The simulations were run in a memory-share workstation; each run took minutes to hours depending on the pressure gradients and heterogeneity of aperture fields. The goal of this study is to assess the linear time-dependence of k [m^2] suggested above for 3D rough fractures and to determine whether it represents a common phenomenon at various reactive transport regimes demonstrated by Peclet and Damkohler numbers. This was achieved by solving the 2D reactive DAM for 3D fractures.

3. Results and discussions

3.1. Impact of fracture heterogeneity on dissolution patterns

The reactivity of calcite induced by acidic brine leads to the fracture wall's dissolution; this generally leads to an expanding aperture field with channelized/preferential dissolution paths demonstrated by the dissolution fingers (Figure 3) and enlarged flux (Figure 4). These preferential dissolution flow paths in turn enhance the concentration gradient acting as a geochemical driving force that further dissolves fractures; this is the driver for self-reinforcing fracture dissolution (Li and Einstein, 2017). The variety of patterns resulting from the potentially self-reinforced dissolution of 3D rough-walled fractures is due to variations in the local Damkohler number (*Da*) defined as:

$$Da = \frac{RL}{\left(C_{eq} - C\right)\boldsymbol{q}} \qquad (9)$$

where L [m] is fracture length (the grid cell size was not used here for calculating *Da* since we are more concerned about the area-averaged <*Da*> [–] as discussed below). The *Da* inherently hinges on the b field and pressure gradient that dictates the magnitude of R, $\boldsymbol{q}$, and C. Here, we only show the dissolution patterns where dissolution fingers are prominent (Figure 3), many other patterns with and without apparent dissolution fingers are not shown here.

For short-range, spatially-correlated fractures, the dissolution fingers gradually became more apparent with increasing <*Da*> (the area-averaged *Da*) (Figures 3a-3f); this observation is congruent with previous studies (Iyer and Elkhoury, 2015; Szymczak and Ladd, 2004). This is because at low pressure gradient with large <*Da*> the localized dissolution fingers keep advancing forward with a strong positive feedback between flow and reaction; this self-reinforcement results in an almost constant finger width (Figures 3c and 3f) - a similar phenomenon was found in partially molten porous media with developed melting channels for magma flow (Jordan and Hesse, 2015). However, for high pressure gradient cases with small <*Da*>, the localized fingers disappear due to the fairly uniform reactivity that widens the aperture field at more or less the same dissolution rate, where the original aperture structure was maintained (Figures 3a and 3d).

A similar trend or pattern, i.e., the preferential dissolution fingers gradually establish, with increasing <*Da*> was also found for fractures with relatively long λ (Figure 3g-3l). Unlike fractures with short λ where dissolution fingers with a relatively uniform spacing developed, dissolution fingers were mostly concentrated in the preferential flow paths determined by connected large aperture zones within the originally unaltered spatially-correlated aperture field; this is again the self-reinforcing mechanism as demonstrated by the focused flux (Figure 4). The number of dissolution fingers was much less and the width was wider in the fractures with long λ than the dissolution fingers in the fractures with short λ (Figure 3). These dissolution patterns agree with previous results (Iyer and Elkhoury, 2015). While $\sigma_b/\langle b \rangle$ affects the self-reinforcing dissolution by altering $\boldsymbol{q}$ and the resultant C, the role of $\sigma_b/\langle b \rangle$ in determining the overall dissolution patterns is trivial compared to the effects caused by λ as discussed before; this was also suggested in Iyer and Elkhoury (2015).

3.2. Linear time-dependence of fracture permeability

In general and aligned with experimental results (Deng et al., 2015; Noiriel et al., 2013), the dissolution of rough fractures in an acidic environment led to a linear time-dependence of *k* (Figures 5-6) across the analyzed Peclet (*Pe* [–]) and <*Da*> number regimes considering a varying degree of reactive transport regimes; the *Pe* and <*Da*> considered were within the validity thresholds theoretically proposed in Wang and Cardenas (2017) regarding the fracture aspect ratio. This linear *k* increase with time persists across different dissolution patterns illustrating a common relationship.

Despite different dissolution patterns, the onset of the linear relationship roughly occurred once the dissolution front reaches the outlet of 3D rough fractures (Figure 5); this was also demonstrated in previous idealized numerical model experiments and laboratory observations (Deng et al., 2015; Fitts and Peters, 2013). The onset of the linear relationship is attributed to the following reasons: (a) the dissolution front migrates and leaves behind an expanding and usually large *b*, (b) the unaltered *b* ahead of the dissolution front is often smaller than the continuously expanding *b*, (c) the narrowest *b* (i.e., the unaltered *b* usually located at the outlet) limits the magnitude of *k* according to the Cubic Law (Witherspoon et al., 1980; Zimmerman et al., 1991). All these factors imply that the bulk *k* remains fairly constant until the unaltered and narrowest *b* located at the outlet expands due to dissolution; this eventually initiates the linear *k* increase with *t*.

After the initiation of the linear relationship between *k* and *t*, we observed a persistent linear time-dependence of *k* (Figures 5 and 6a) for 3D rough fractures with varying σ_b/<*b*> and λ regarding varying degrees of dissolution patterns in response to different reactive transport regimes. This is however beyond our expectation because the theory of the linear time-dependence was developed based on 2D fractures (i.e., parallel plates) with a single flow channel which is essentially a straight a line when viewed orthogonally from the fracture plane, so everything is forced to flow along this line only (Wang and Cardenas, 2017). Unlike 2D fractures, the flow field in 3D rough fractures is far more complex and is potentially characterized by multiple preferential flow curves from the top orthogonal view rather than a single line (Elkhoury et al., 2013); this may lead to violation of the linear relationship theory. However, our numerical experiments within 3D fractures demonstrated that the collective flow behavior with possible multiple flow channels (Figure 5) is identical to that for a single flow channel, i.e., k increases linearly with time due to self-reinforcement. This was also identified in physical experiments for 3D rough fractures (Deng et al., 2015). This similarity in k evolution holds because the main conduits in 3D fractures exhibiting positive feedback between flow and transport dominate over smaller channels in terms of flux (Figure 4). That is, the dominant conduits in 3D fractures behave in a similar way as the single channel in 2D fractures. The theory of the linear relationship based on a 2D idealized model is therefore applicable for describing the k evolution of 3D rough fractures with more complex flow patterns and phenomena such as channelization.

To further interrogate the common occurrence of linear time-dependence of k, we quantified the time rate of change of permeability (k/t) based on the slope of $k(t)$ curves (Figure 6a). The slope was computed and chosen once the linear relationship manifested over 200 simulation time steps. To exclude the effect of $<b>$, we created and conducted simulations through two sets of fractures with different $<b>$; each set of given $<b>$ had the same range of $\sigma_b/<b>$ and λ/L. Not surprisingly and regardless of Pe and $<Da>$ (i.e., different reactive transport regimes), all k/t are on the order of magnitude of 10^{-12} m^2/s with a median value ($\sim 1.3\times 10^{-12}$ m^2/s) that is slightly greater than the theoretical value of 1.07×10^{-12} m^2/s according to equation (8) (Figure 6b). This also holds true for the two sets of $<b>$ (results are indistinguishable in

Figure 6b). The narrow variations in *k*/*t* might be attributed to the *Sh* because it is dependent on fracture geometry (Kays et al., 2012). The aperture fields and main flow conduits were expanding over the course of the dissolution process (Figures 3 and 5) and thus *Sh* was slightly varying.

Aside from slight variations in *k*/*t* caused by variation in *Sh*, the slope of *k*/*t* also depends on the concentration difference according to equation (8). This difference is related to the acidity of brine (e.g., pH values under different supercritical CO_2 pressures). Our simulations employed a constant concentration ($[Ca^{2+}]$) that was based on previous experiments (Elkhoury et al., 2013) and thus excluded the concentration effects. Deng et al. (2015)'s experiments explored the calcite fracture's dissolution patterns at high and low supercritical CO_2 pressures. They found that the saturated $[Ca^{2+}]$ varied in response to the CO_2 solubility induced by different CO_2 pressures. We calculated *k*/*t* by estimating the right hand term in equation (8); these calculations considered the effects of CO_2 pressures on C_{eq} that was derived from effluent concentration. Although C_{eq} was variable, Deng et al.'s two experiments all confirmed a linear time-dependence of *k* and the experimentally-derived *k*/*t* were equally close to 1.8×10^{-12} m^2/s, whose value is slightly higher than the median value ($\sim1.3\times10^{-12}$ m^2/s) based on our numerical experiments (Figure 6b). The *k*/*t* derived by different methods, including theory, physical experiments, and numerical simulations, are on the same order of magnitude albeit with up to 30% difference between them. This fact not only confirms the common occurrence of linear time-dependence of *k* for 3D rough fractures at varying reactive transport regimes, but also demonstrates the robustness of the DAM in capturing *k* evolution in a self-reinforcing reactive environment.

4. Implications

The subsurface injection of CO_2 promotes both the dissolution and precipitation of minerals within and around the CO_2 plume (Altman et al., 2014; Steefel et al., 2013). In the case of fractured calcite or acid-soluble caprock, the migration of CO_2-saturated brine could lead to either self-sealing or self-reinforcing phenomena depending on the supply of acidic fluid. In the worst case with a persistent source of acidic fluid, e.g., CO_2 and brine two-phase flow (Fitts and Peters, 2013), our study implies that the acidic fluid migration can promote the fractured calcite dissolution with increasing k and flux over time; this might compromise the subsurface CO_2 storage in a relatively shorter time than expected. Note that our simulations only considered a pure calcite matrix. For fractures containing relatively inert materials (quartz, clay, etc.), the extent of permeability increase is limited by the residual materials in the fractures. It may even be the case that these residual materials are mobilized during calcite dissolution and migrate downstream resulting in clogging and a decrease in fracture permeability. These scenarios are beyond the scope of this study.

Although our study focused on the fracture dissolution at the single fracture scale, the evolving k path observed in our simulations was proposed to manifest at the field scale. An appropriate example is karst conduit development (Andre and Rajaram, 2005) wherein a slow continuous k increase is followed by an rapid k increase due to the positive feedback between flow and reactive transport processes in a H_2O-CO_2-$CaCO_3$ system. The k evolution could also be vital for mass transport in many other self-reinforcing systems, including partially-molten magma flow in porous media (Hewitt, 2010; Jordan and Hesse, 2015) and warm water flowing through fractured ice (Das et al., 2008).

5. Conclusion

We simulated flow and reactive transport processes for dissolving three-dimensional rough fractures using a two-dimensional depth-averaged model. In this self-reinforcing dissolution system, the fracture expands followed by mass flux increase. This leads to an increasing geochemical driving force that further dissolves the fracture. Based on numerical simulations through rough-walled fractures with different roughness and aperture field correlation length, we observed a persistent linear time-dependence of fracture permeability (*k*) after the dissolution front reaches the fracture outlet. This linear relationship between *k* and time (*t*) holds across a range of Peclet and Damkohler numbers which correspond to different dissolution patterns from distributed, evenly-spaced fingers to very focused flows with a dominant channel. The linear time-dependence of *k* is consistent with experimental observations. The estimated time rate of change of *k* (i.e., *k*/*t*) further illustrates the linear relationship between *k* and *t*. *k*/*t* is on the same order of magnitude for all the studied fractures despite their varying degrees of dissolution patterns. Our numerical model-derived *k*/*t* values for rough fractures at varying reactive transport regimes are consistent with values based on carefully-designed experiments and on theory for idealized two-dimensional geometry. All these collectively suggest the common presence of linear fracture permeability increase with time due to self-reinforcing dissolution.

Acknowledgments

This work is supported as part of the Center for Frontiers of Subsurface Energy Security (CFSES) at the University of Texas at Austin, an Energy Frontier Research Center funded by the U.S. Department of Energy, Office of Science, Office of Basic Energy Sciences under award DE-SC0001114. Additional support was provided by the Geology Foundation of the University of Texas and Tianjin University. All model results have been made available in the figures.

References

Altman, S.J., 2014 Aminzadeh, B., Balhoff, M.T., Bennett, P.C., Bryant, S.L., Cardenas, M.B., Chaudhary, K., Cygan, R.T., Deng, W., Dewers, T., DiCarlo, D.A., Eichhubl, P., Hesse, M.A., Huh, C., Matteo, E.N., Mehmani, Y., Tenney, C.M., Yoon, H.

Chemical and Hydrodynamic Mechanisms for Long-Term Geological Carbon Storage.

J. Phys. Chem. C, 118(2014), pp. 15103-15113, 10.1021/jp5006764.

Andre, B.J., 2005 Rajaram, H.

Dissolution of limestone fractures by cooling waters: Early development of hypogene karst systems.

Water Resour. Res., 41(2005), 10.1029/2004WR003331.

Aris, R., 1956.

On the Dispersion of a Solute in a Fluid Flowing through a Tube.

P. Roy. Soc. Lond. A. Mat., 235(1956), pp. 67-77, 10.1098/rspa.1956.0065.

Berkowitz, B., 2002.

Characterizing flow and transport in fractured geological media: A review.

Adv. Water Resour., 25(2002), pp. 861-884, 10.1016/s0309-1708(02)00042-8.

Brush, D.J., 2003 Thomson, N.R.

Fluid flow in synthetic rough-walled fractures: Navier-Stokes, Stokes, and local cubic law simulations.

Water Resour. Res., 39(2003), pp. 1085, 10.1029/2002wr001346.

Candela, T., 2012 Renard, F., Klinger, Y., Mair, K., Schmittbuhl, J., Brodsky, E.E.

Roughness of fault surfaces over nine decades of length scales.

J. Geophys. Res.-Sol. Ea., 117(2012), B08409, B0840910.1029/2011jb009041.

Das, S.B., 2008 Joughin, I., Behn, M.D., Howat, I.M., King, M.A., Lizarralde, D., Bhatia, M.P.

Fracture Propagation to the Base of the Greenland Ice Sheet During Supraglacial Lake Drainage.

Science, 320(2008), pp. 778-781, 10.1126/science.1153360.

Deng, H., 2015 Fitts, J.P., Crandall, D., McIntyre, D., Peters, C.A.

Alterations of Fractures in Carbonate Rocks by CO_2-Acidified Brines.

Environ. Sci. Technol., 49(2015), pp. 10226-10234, 10.1021/acs.est.5b01980.

Detwiler, R.L., 2007 Rajaram, H.

Predicting dissolution patterns in variable aperture fractures: Evaluation of an enhanced depth-averaged computational model.

Water Resour. Res., 43(2007), W0440310.1029/2006wr005147.

Elkhoury, J.E., 2013 Ameli, P., Detwiler, R.L.

Dissolution and deformation in fractured carbonates caused by flow of CO_2-rich brine under reservoir conditions.

Int. J. Greenh. Gas Con., 16(2013), pp. S203-S215, 10.1016/j.ijggc.2013.02.023.

Fitts, J.P., 2013 Peters, C.A.

Caprock fracture dissolution and CO2 leakage.

Rev. Mineral. Geochem., 77(2013), pp. 459-479, 10.2138/rmg.2013.77.13.

Ge, S., 1997.

A governing equation for fluid flow in rough fractures.

Water Resour. Res., 33(1997), pp. 53-61, 10.1029/96wr02588.

Hewitt, I.J., 2010.

Modelling melting rates in upwelling mantle.

Earth Planet. Sci. Lett., 300(2010), pp. 264-274, 10.1016/j.epsl.2010.10.010.

Huerta, N.J., 2012 Hesse, M.A., Bryant, S.L., Strazisar, B.R., Lopano, C.L.

Experimental evidence for self-limiting reactive flow through a fractured cement core: Implications for time-dependent wellbore leakage.

Environ. Sci. Technol., 47(2012), pp. 269-275, 10.1021/es3013003.

Iyer, J., 2015 Elkhoury, J.E.

Effect of Fracture Heterogeneities on Reactive Flow.

49th US Rock Mechanics/Geomechanics Symposium. American Rock Mechanics Association.

Jordan, J.S., 2015 Hesse, M.A.

Reactive transport in a partially molten system with binary solid solution.

Geochem. Geophy. Geosy., 16(2015), pp. 4153-4177, 10.1002/2015GC005956.

Kampman, N., 2016 Busch, A., Bertier, P., Snippe, J., Hangx, S., Pipich, V., Di, Z., Rother, G., Harrington, J.F., Evans, J.P., Maskell, A., Chapman, H.J., Bickle, M.J.

Observational evidence confirms modelling of the long-term integrity of CO2-reservoir caprocks.

Nat. Commun., 7(2016), 12268, 10.1038/ncomms12268.

Kang, P.K., 2016 Brown, S., Juanes, R.

Emergence of anomalous transport in stressed rough fractures.

Earth Planet. Sci. Lett. 454(2016), pp. 46-54. 10.1016/j.epsl.2016.08.033.

Kays, W.M., 2012 Crawford, M.E., Weigand, B.

Convective heat and mass transfer.

Tata McGraw-Hill Education.

Li, W., 2017 Einstein, H. H.

Theoretical and Numerical Investigation of the Cavity Evolution in Gypsum Rock.

Water Resour. Res., 53(2017), pp. 9988-10001. 10.1002/2017WR021776

Nicholl, M.J., 1999 Rajaram, H., Glass, R.J., Detwiler, R.

Saturated flow in a single fracture: evaluation of the Reynolds Equation in measured aperture fields.

Water Resour. Res., 35(1999), pp.3361-3373, 10.1029/1999wr900241.

Noiriel, C., 2013 Gouze, P., Madé, B..

3D analysis of geometry and flow changes in a limestone fracture during dissolution.

J. Hydrol. 486 (2013), pp. 211-223, 10.1016/j.jhydrol.2013.01.035.

Pokrovsky, O.S., 2009 Golubev, S.V., Schott, J., Castillo, A.

Calcite, dolomite and magnesite dissolution kinetics in aqueous solutions at acid to circumneutral pH, 25 to 150 C and 1 to 55 atm pCO_2: New constraints on CO_2 sequestration in sedimentary basins.

Chem. Geol., 265(2009), pp. 20-32,10.1016/j.chemgeo.2009.01.013.

Pyrak-Nolte, L.J., 2016 Nolte, D.D.

Approaching a universal scaling relationship between fracture stiffness and fluid flow.

Nat. Commun., 7(2016), pp. 10663, 10.1038/ncomms10663.

Remy, N., 2009 Boucher, A., Wu, J.

Applied geostatistics with SGeMS: A user's guide.

Cambridge University Press.

Renshaw, C.E., 1995.

On the relationship between mechanical and hydraulic apertures in rough-walled fractures.

J. Geophys. Res.: Sol. Ea., 100(1995), pp. 24629-24636, 10.1029/95jb021596.

Starchenko, V., 2016 Marra, C.J., Ladd, A.J.C.

Three-dimensional simulations of fracture dissolution.

J. Geophys. Res.-Sol. Ea., 121(2016), pp. 6421-6444, 10.1002/2016JB013321.

Steefel, C.I., 2013 Molins, S., Trebotich, D.

Pore scale processes associated with subsurface CO2 injection and sequestration.

Rev. Mineral. Geochem., 77(2013), pp. 259-303, 10.2138/rmg.2013.77.8.

Szymczak, P., 2004 Ladd, A.J.C.

Microscopic simulations of fracture dissolution.

Geophys. Res. Lett., 31(2004), pp. L23606, 10.1029/2004gl021297.

Szymczak, P., 2012 Ladd, A.J.C.

Reactive-infiltration instabilities in rocks. Fracture dissolution.

J. Fluid Mech., 702(2012), pp. 239-264, 10.1017/jfm.2012.174.

Taylor, G., 1953.

Dispersion of Soluble Matter in Solvent Flowing Slowly through a Tube.

P. Roy. Soc. Lond. A. Mat., 219(1953), 186-203, doi: 10.1098/rspa.1953.0139.

Wang, L., 2016 Cardenas, M.B.

Development of an empirical model relating permeability and specific stiffness for rough fractures from numerical deformation experiments.

J. Geophys. Res.-Sol. Ea., 121(2016), pp. 4977-4989, 10.1002/2016JB013004.

Wang, L., 2017 Cardenas, M.B.

Linear permeability evolution of expanding conduits due to feedback between flow and fast phase change.

Geophys. Res. Lett., 44(2017), pp. 4116-4123, 10.1002/2017gl073161.

Wang, L., 2012 Cardenas, M.B., Deng, W., Bennett, P.C.

Theory for dynamic longitudinal dispersion in fractures and rivers with Poiseuille flow.

Geophys. Res. Lett., 39(2012), pp. L05401, 10.1029/2011gl050831.

Wang, L., 2015 Cardenas, M.B., Slottke, D.T., Ketcham, R.A., Sharp, J.M.

Modification of the Local Cubic Law of fracture flow for weak inertia, tortuosity, and roughness.

Water Resour. Res., 51(2015), pp. 2064-2080, 10.1002/2014WR015815.

Witherspoon, P.A., 1980 Wang, J.S.Y., Iwai, K., Gale, J.E.

Validity of Cubic Law for fluid flow in a deformable rock fracture.

Water Resour. Res., 16(1980), pp. 1016-1024, 10.1029/WR016i006p01016.

Zimmerman, R.W., 2004 Al-Yaarubi, A., Pain, C.C., Grattoni, C.A.

Non-linear regimes of fluid flow in rock fractures.

Int. J. Rock Mech. Min., 28(2014), pp. 325-331, 10.1016/0148-9062(91)90597-f.

Zimmerman, R.W., 1991 Kumar, S., Bodvarsson, G.S.

Lubrication theory analysis of the permeability of rough-walled fractures.

Int. J. Rock Mech. Min., 41(1991), Supplement 1(0), pp. 163-169, 10.1016/j.ijrmms.2004.03.036.

Figure Captions

Figure 1. Examples of log-normally distributed aperture fields across a broad range of roughness ($0.1 <= \sigma_b/<b> <= 1.6$) and dimensionless correlation length ($0.01 =< \lambda/L <= 1$), where b is the aperture field with standard deviation σ_b and arithmetic mean $<b>$, λ is the correlation length of the b field, and L is total fracture length and width. The right column shows the relative frequency distribution of the aperture field corresponding to similarly colored outlines for the fields. Note that the right column plots are for the log-normally distributed aperture fields, where the integrated area under each of the curve increases with roughness.

Figure 2. Conceptual diagram of two-dimensional, depth-averaged model for fluid flow and reactive transport in a rough-walled fracture. The colors represent the aperture magnitude, fluid flow boundary conditions are in red, transport boundary conditions are in blue, and white arrow indicates the mean flow direction driven by the pressure gradient ∇p.

Figure 3. Aperture dissolution patterns for four fractures with increasing dimensionless correlation lengths (λ/L) from top to bottom at time = 1000 initial pore volume; each column represents different area-averaged Damkohler numbers ($<Da>$) with the increasing pressure gradient ∇p from left to right. λ is the aperture correlation length, L is total fracture length, the initial pore volume = volume / flux at time = 0, and Da is defined in equation (9).

Figure 4. Self-reinforcing dissolution patterns with channelized streamlines (red) over time for two fractures with increasing dimensionless correlation length (λ/L) from top to bottom. λ is the aperture correlation length, L is total fracture length, and the initial pore volume PV_0= volume /

flux at time = 0. The streamlines connect the fluid path from the inlet to outlet, where flux is the same in the region between streamlines. The tortuous flow path with a zigzag shape (especially in the first column) is due to the fluid flowing in the undissolved fracture zone with randomly-distributed apertures. The number of streamlines depends on the total flux which increases over time.

Figure 5. Linear permeability increase (blue line) with time through 3D rough fractures as exemplified by a) λ/L=0.01, $\sigma_b/<b>$=0.8 and b) λ/L=0.6, $\sigma_b/<b>$=0.4, where b is the aperture field with standard deviation σ_b and arithmetic mean $<b>$, λ is the aperture correlation length, and L is total fracture length. Insets show the dissolution patterns = expanding aperture field – the initial aperture field.

Figure 6. The linear relationship between permeability (k) and time (t) across a range of Peclet number (Pe=10^2~10^5), area-averaged Damkohler number ($<Da>$=10^{-1}~10^3), fracture roughness ($\sigma_b/<b>$ =0.1~1.6), and aperture field correlation length (λ =0.1L ~ 1L). This linear relationship is demonstrated by: a) linear dimensionless permeability (k/k_0) increase with dimensionless time for all studied fractures, and b) small range in the time rate of change of k (k/t) as demonstrated by a histogram of k/t. k_0 is permeability (k) at t = 0, initial pore volume = volume/flux at t = 0, $Pe=q/D_m$, q is fluid flux, D_m is molecular diffusion coefficient, Da is defined in equation (9), Sh is Sherwood Number that is constant for given geometry, b is the aperture field with standard deviation σ_b and arithmetic mean $<b>$, and L is total fracture length. The dashed line is the theoretical value (k/t = 1.07×10^{-12} m^2/s) according to equation (8).

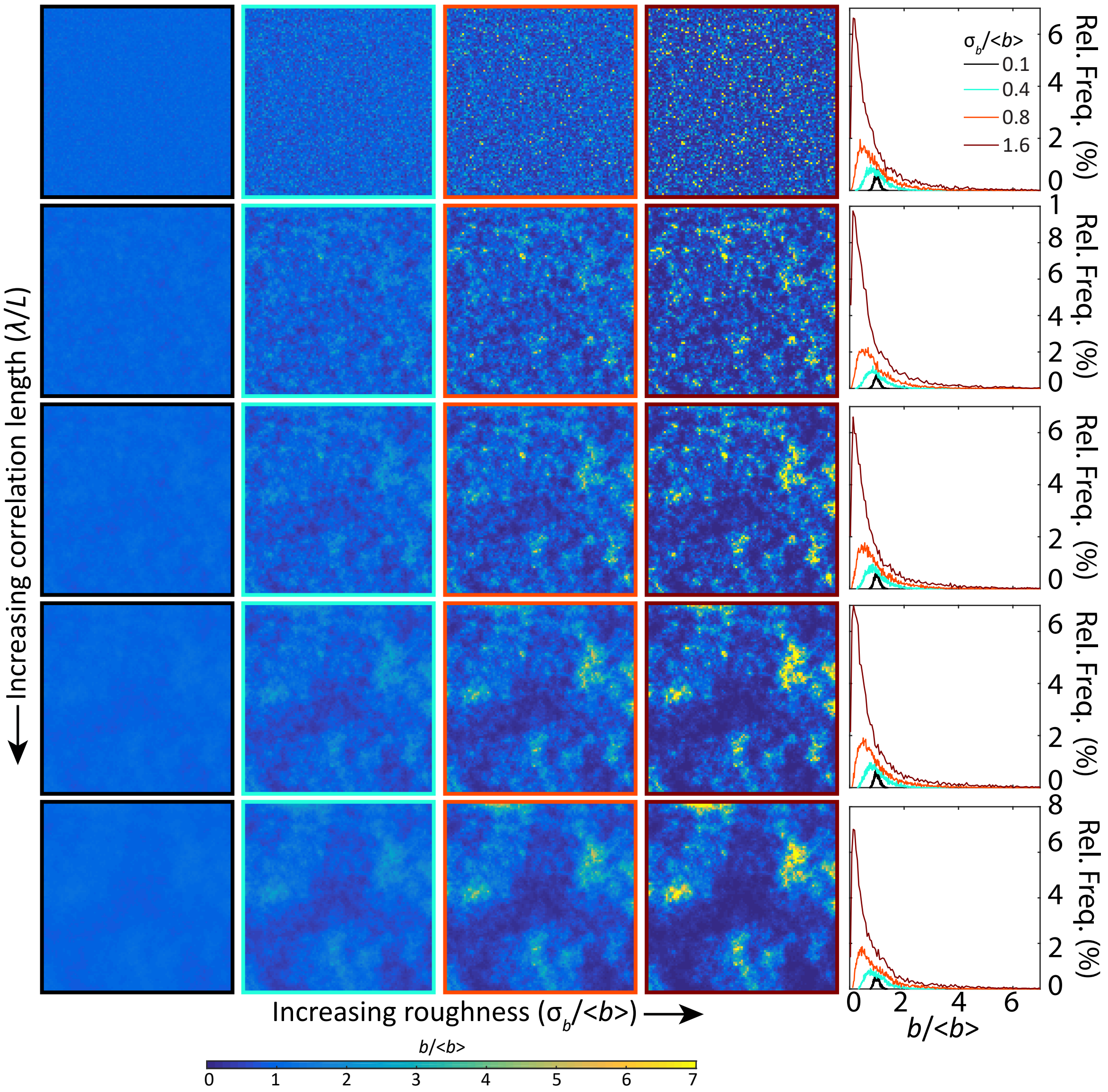
Increasing correlation length (λ/L)
Increasing roughness (σ_b/<b>)
b/<b>
0
1
2
3
4
5
6
7
σ_b/<b>
0.1
0.4
0.8
1.6
Rel. Freq. (%)
0
2
4
6
8
10
b/<b>

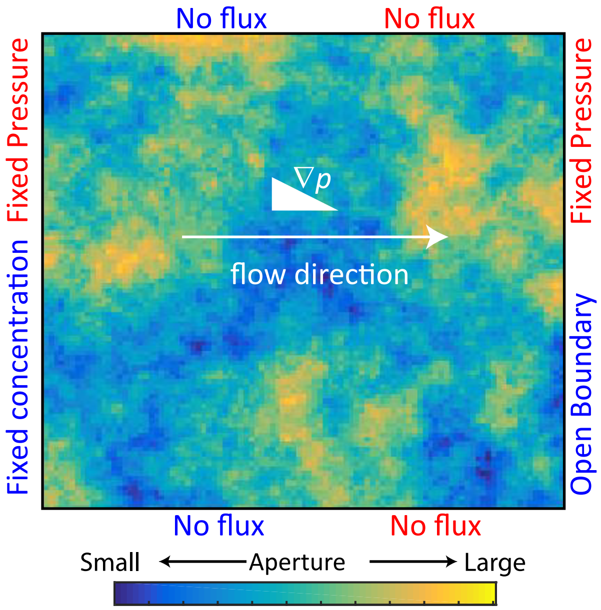
No flux
No flux
Fixed Pressure
Fixed Pressure
∇p
flow direction
Fixed concentration
Open Boundary
No flux
No flux
Small
Aperture
Large

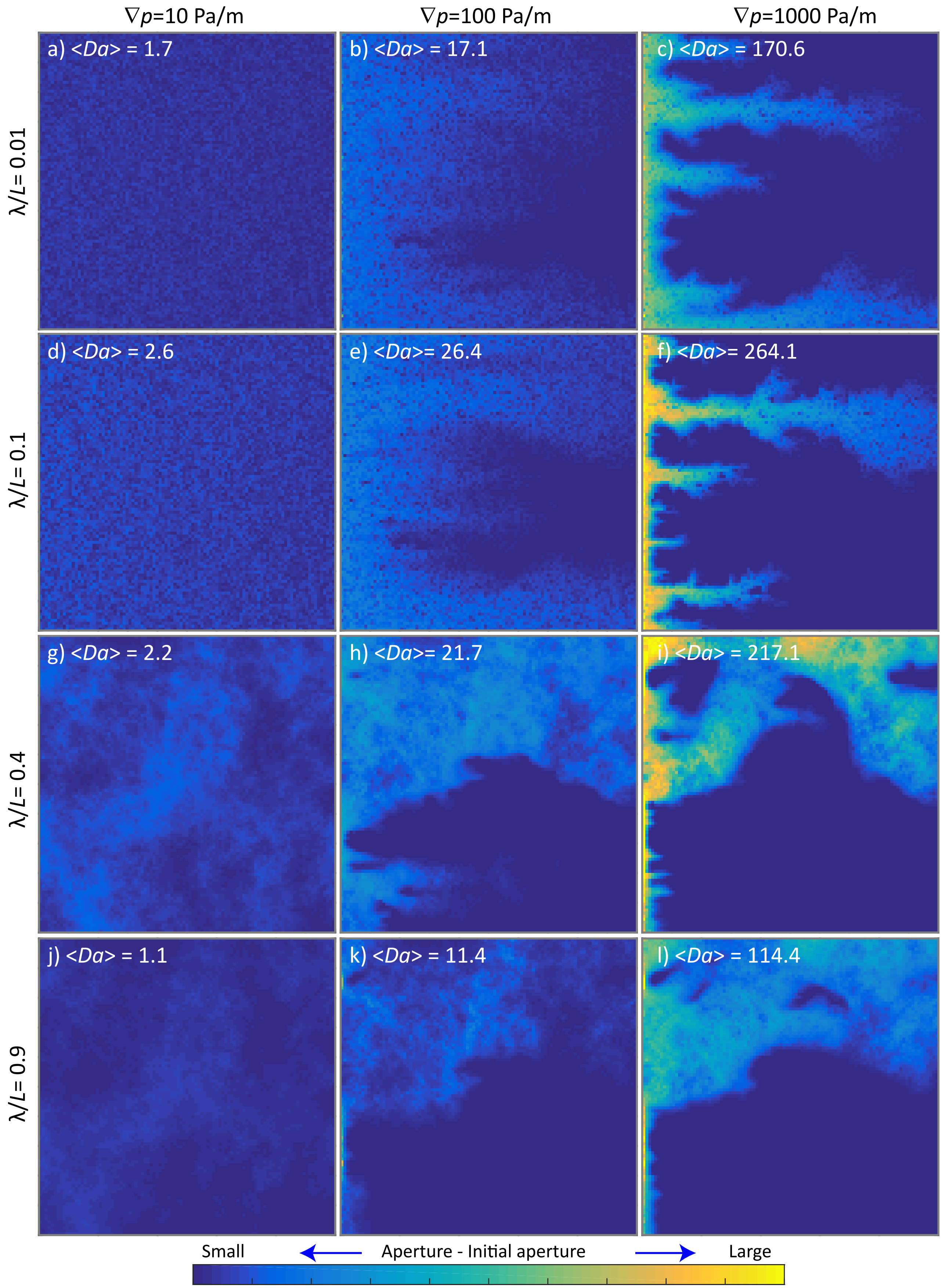
∇p=10 Pa/m
∇p=100 Pa/m
∇p=1000 Pa/m
λ/L= 0.01
a) <Da> = 1.7
b) <Da> = 17.1
c) <Da> = 170.6
λ/L= 0.1
d) <Da> = 2.6
e) <Da>= 26.4
f) <Da>= 264.1
λ/L= 0.4
g) <Da> = 2.2
h) <Da>= 21.7
i) <Da> = 217.1
λ/L= 0.9
j) <Da> = 1.1
k) <Da> = 11.4
l) <Da> = 114.4
Small
Aperture - Initial aperture
Large

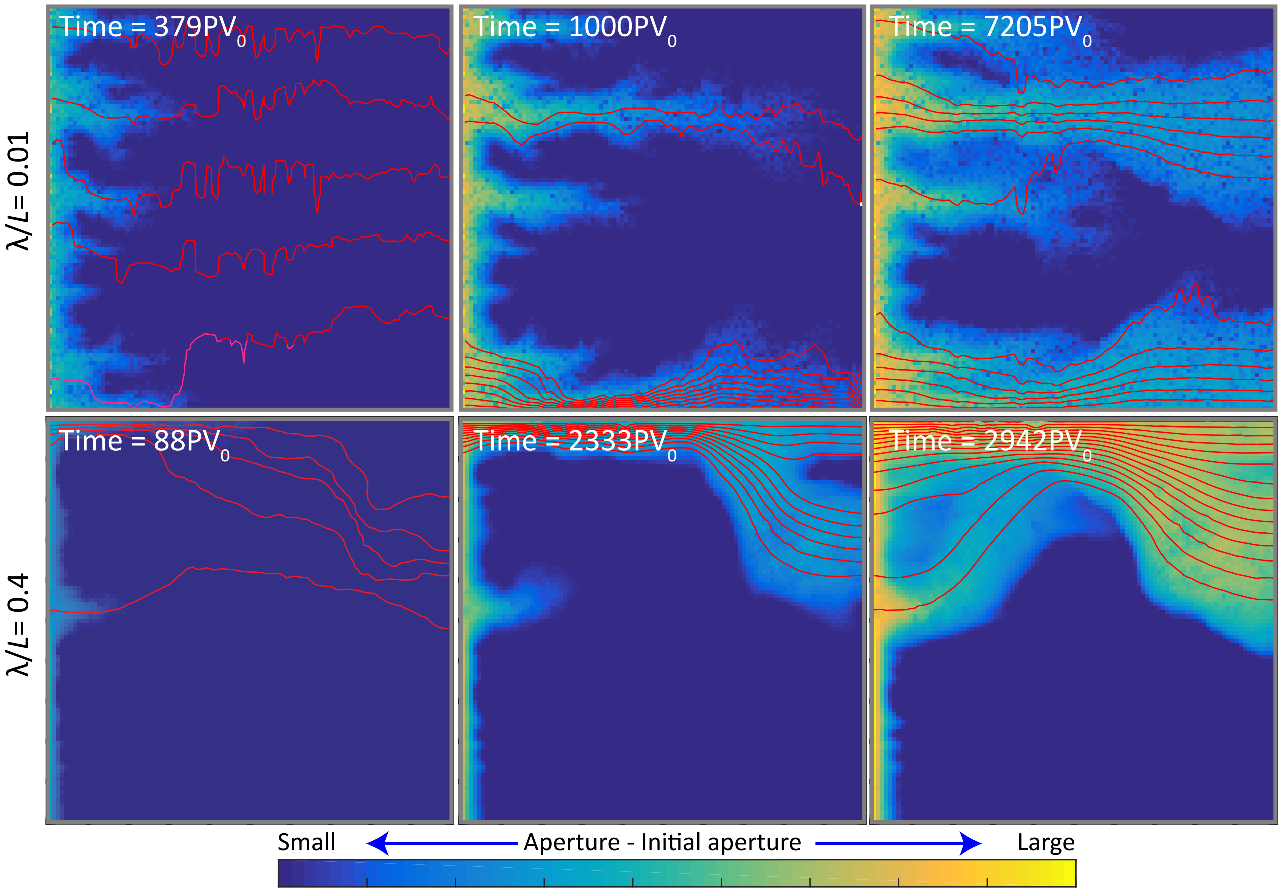
λ/L= 0.01
λ/L= 0.4
Time = 379PV_0
Time = 1000PV_0
Time = 7205PV_0
Time = 88PV_0
Time = 2333PV_0
Time = 2942PV_0
Small
Aperture - Initial aperture
Large

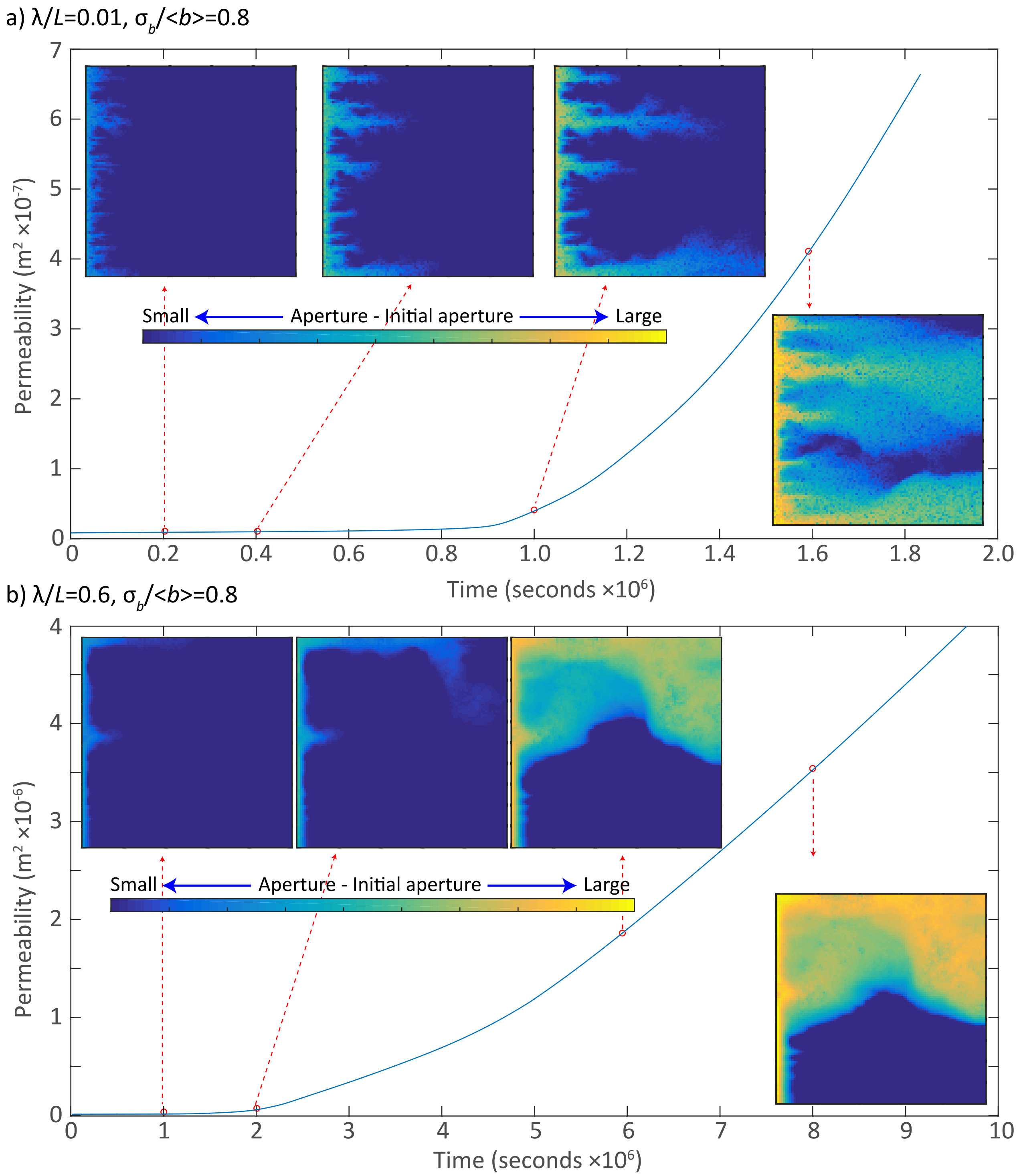
a) λ/L=0.01, σ_b/<b>=0.8
Permeability (m² ×10⁻⁷)
0
1
2
3
4
5
6
7
Small
Aperture - Initial aperture
Large
0
0.2
0.4
0.6
0.8
1.0
1.2
1.4
1.6
1.8
2.0
Time (seconds ×10⁶)
b) λ/L=0.6, σ_b/<b>=0.8
Permeability (m² ×10⁻⁶)
0
1
2
3
4
Small
Aperture - Initial aperture
Large
0
1
2
3
4
5
6
7
8
9
10
Time (seconds ×10⁶)

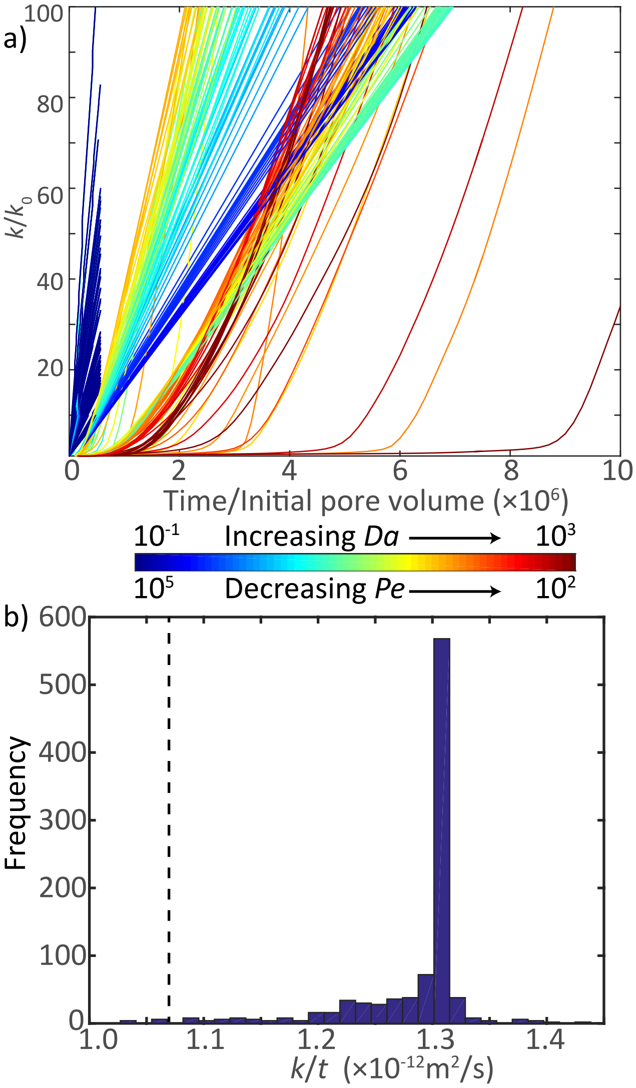
a)
100
80
60
40
20
k/k0
0
2
4
6
8
10
Time/Initial pore volume (×10^6)
10^-1
Increasing Da
10^3
10^5
Decreasing Pe
10^2
b)
600
500
400
300
200
100
0
Frequency
1.0
1.1
1.2
1.3
1.4
k/t (×10^-12 m^2/s)